Journal of Systems Engineering and Electronics
Vol. 31, No. 3, June 2020, pp.488 – 499

Particle swarm optimization for rigid body reconstruction after micro-Doppler removal in radar analysis

LI Hongzhi[1,2] and WANG Yong[1,2,*]

1. School of Electronics and Information Engineering, Harbin Institute of Technology, Harbin 150001, China;
2. Key Laboratory of Marine Environmental Monitoring and Information Processing, Ministry of Industry and Information Technology, Harbin 150001, China

Abstract: The rotating micro-motion parts produce micro-Doppler (m-D) effects which severely influence the quality of inverse synthetic aperture radar (ISAR) imaging for complex moving targets. Recently, a method based on short-time Fourier transform (STFT) and L-statistics to remove m-D effects is proposed, which can separate the rigid body parts from interferences introduced by rotating parts. However, during the procedure of removing m-D parts, the useful data of the rigid body parts are also removed together with the m-D interferences. After summing the rest STFT samples, the result will be affected. A novel method is proposed to recover the missing values of the rigid body parts by the particle swarm optimization (PSO) algorithm. For PSO, each particle corresponds to a possible phase estimation of the missing values. The best particle is selected which has the minimal energy of the side lobes according to the best fitness value of particles. The simulation and measured data results demonstrate the effectiveness of the proposed method.

Keywords: micro-Doppler (m-D), inverse synthetic aperture radar (ISAR), L-statistics, particle swarm optimization (PSO).

DOI: 10.23919/JSEE.2020.000023

1. Introduction

During the inverse synthetic aperture radar (ISAR) imaging, the effect induced by rotating parts of targets attracks high attention [1 – 7]. From the point of signal processing, the rotating parts introduce sinusoidal frequency modulation signals in azimuth echoes, which influence the ISAR imaging of rigid bodies. Therefore, the separation of the micro-Doppler (m-D) parts and rigid parts is studied extensively [8 – 12]. In recent years, the solution to solving the m-D effect is proposed by many researchers. Among them, Stankovic et al. [13] proposed a new method based on short-time Fourier transform (STFT) and L-statistics, which is practical and simple to separate the rigid bodies from rotating parts. Because the non-rigid parts introduce sinusoidal frequency modulation signals and rigid parts introduce constant frequency signals, we can clearly separate them in the time frequency (TF) plane. In the TF domain, as in [13], the STFT samples were sorted by the absolute values for each frequency, then the appropriate percentage of the highest STFT values were removed. After the process above, the sinusoidal frequency modulation signals can be removed. Then, by summing the rest STFT samples, it is easy to get the Fourier transform (FT) of the rigid bodies. This method is proved easier to apply than other methods [8 – 12]. Then the genetic algorithm (GA) is used to restore the missing values of rigid bodies [14], because some useful data of rigid bodies are removed during the procedure of removing the non-rigid parts [13]. However, the computational cost of the GA method is very high because of the complex process of encoding, crossover, mutation and decoding. Moreover, the initial generation proposed in [14] cannot consider all the possible solutions. In [14], each individual represented the phase of the rigid body's missing data, but the paper only considered the phase in the set $[0, \frac{1}{8}\pi, \frac{2}{8}\pi, \frac{3}{8}\pi, \frac{4}{8}\pi, \frac{5}{8}\pi, \frac{6}{8}\pi, \frac{7}{8}\pi]$. Therefore, for eliminating m-D effects better, a novel method based on the particle swarm optimization (PSO) algorithm is proposed to estimate and recover the missing values of the rigid bodies.

The PSO as an evolutionary algorithm is widely used in the field of the optimization problem [15 – 17]. The algorithm was firstly proposed in [15]. Its basic idea comes from the hunting behavior acted by birds. The method starts with an initial population including some certain amount of particles, where each particle represents a possible solution to the problem to be solved. Then, by constantly changing the velocity and position, each particle's position can be optimal in the history and the whole popu-

Manuscript received April 29, 2019.
*Corresponding author.
This work was supported by the National Natural Science Foundation of China (61622107; 61871146).

lation can also find its best position. The optimal position of the population is the fittest solution to the actual problem.

Under the background of the proposed method removing non-rigid parts, each particle is the possible solution of the phase values of the missing rigid body points. As in [14], in the same frequency bin, we can set the amplitudes of the removed STFT values close to rigid parts as the median of the rest STFT values. In this paper, to estimate the missing values' phases, we choose the initial population in PSO randomly within the set $[0, 2\pi)$ for each particle.

This paper is organized as follows. The STFT and L-statistics based method is shown in Section 2. The PSO algorithm for the construction of missing data close to the rigid body is proposed in Section 3. The signal simulation results and measured data processing results are shown in Section 4. Section 5 concludes this paper.

2. m-D removal based on STFT and L-statistics

2.1 Radar signal with rotating part modeling

In [13], the received discrete signal of continuous wave (CW) radar, including both the rotating part points and the rigid body points, could be given as follows:

$$s(m) \cong \sum_{i=1}^{K} \sigma_{Bi} \mathrm{e}^{\mathrm{j}y_{Bi}m} + \sum_{i=1}^{Q} \sigma_{Ri} \mathrm{e}^{\mathrm{j}[y_{R0i}m + A_{Ri}\sin(\omega_{Ri}m+\varphi_i)]} \quad (1)$$

where $m = 0, \ldots, M-1$, the amount of the rigid body points is K, and the amount of the rotating points is Q. Respectively, the reflection coefficients are presented as σ_{Bi} and σ_{Ri}. y_{Bi} and y_{R0i} are proportional to the position of the rigid body reflector and the rotation center, respectively. A_{Ri} is proportional to the distance between the rotating point and the rotation center, while ω_{Ri} is the rotation rate of each rotating point.

2.2 Method description of STFT and L-statistics

In [13], the signal with constant frequency and the sinusoidal frequency modulation (FM) signals had different TF distributions after STFT, thus they could be separated. The STFT results of signal $s(i)$ is shown as follows:

$$\mathrm{STFT}(m,k) = \sum_{i=1}^{M-1} s(i) w(i-m) \mathrm{e}^{-\mathrm{j}2\pi ik/M}. \quad (2)$$

In (2), we introduce the window function $w(i)$ for truncating the considered signal. After summing all STFT values, the FT of the original signal $s(i)$ is obtained. Then, the FT's frequency grid and the STFT's are the same, thus, the FT can be reconstructed from it, the reconstruction is defined as follows:

$$\sum_{m=0}^{M-1} \mathrm{STFT}(m,k) = \sum_{i=0}^{M-1} s(i) \left[\sum_{m=0}^{M-1} w(i-m) \right] \mathrm{e}^{-\mathrm{j}2\pi ik/M} = \sum_{i=0}^{M-1} s(i) w_1(i) \mathrm{e}^{-\mathrm{j}2\pi ik/M} = S_{w_1}(k). \quad (3)$$

In (3), the resulting window $w_1(i)$ is constant. Then, for any used window $w(i)$, we get a pure rectangular window $w_1(i)$. We can get the FT result of $s(i)$ by summing all STFT values of signal $s(i)$.

In the method based on STFT and L-statistics, the core idea to separate the rigid bodies from the rotating parts is STFT samples sorting along the time dimension [14]. Generally speaking, the returned signal of the rigid body is stationary, whose frequency is constant in the TF domain, thus the distribution of STFT samples will not be significantly changed after the sorting process. However, the sinusoidal signal produced by the rotating parts is highly non-stationary. As a result, we can eliminate most m-D effects after removing some highest samples of the sorted STFT. Finally, we can sum the rest STFT samples to get the reconstructed data of the rigid body parts.

For a fixed frequency k, assuming that we have a set of STFT with M elements:

$$S_k(m) = \{\mathrm{STFT}(m,k), m = 0, 1, \ldots, M-1\}. \quad (4)$$

We can obtain a new set expressed as $\chi_k(m)$ by sorting $S_k(m)$ for each frequency bin, and $|\chi_k(0)| \leqslant |\chi_k(1)| \leqslant \cdots \leqslant |\chi_k(M-1)|$, $\chi_k(m) \in S_k(m)$. For using the whole set, we can get the following result by summing all STFT samples.

$$\sum_{m=0}^{M-1} \mathrm{STFT}(m,k) = \sum_{m=0}^{M-1} \chi_k(m) = S_{w_1}(k) \quad (5)$$

For each frequency k, after removing $M - M_P$ of the strongest values of $\chi_k(m)$, we can obtain L-statistics [18] form of $S_{w_1}(k)$.

$$S_L(k) = \sum_{m=0}^{M_P-1} \chi_k(m) \quad (6)$$

In (6), $M_P = \mathrm{int}[M((1-T_{per})/100)]$, and the removed samples' percentage is expressed as T_{per}.

As proposed in [19], the basic procedures of rigid body separation based on STFT and L-statistics are shown below.

Step 1 Calculate STFT values of the complex return signal as (2). Then, original complex signals are converted from the time domain to the TF domain after STFT.

Step 2 Sort the STFT result's absolute values from the smallest to the largest for each frequency bin in the TF domain.

Step 3 Set T_{per} as an adaptive value, such as 50%, and then remove the highest value part T_{per} of the sorting STFT results in the TF domain.

Step 4 Sum the remaining STFT results to get the rigid body.

3. Rigid body reconstruction method based on PSO

3.1 PSO algorithm for the missing STFT value estimation

The PSO algorithm is widely used in many optimization procedures, especially when we need to search the optimal solution in multi-dimensional space [20,21].

The mathematical expression of the PSO algorithm is shown below.

Assume a search space with D dimensions, the whole number of particles of the initial population is N. The position of the ith particle is defined as $X_i = (x_{i1}, x_{i2}, \ldots, x_{iD})$, and the changing rate of the position (velocity) of the ith particle for the dth dimension is

$$v_{id}(t+1) = u \cdot v_{id}(t) + c_1 \cdot \mathrm{rand}()[p_{id}(t) - x_{id}(t)] + c_2 \cdot \mathrm{rand}()[p_{gd}(t) - x_{id}(t)]. \tag{7}$$

The changing position can be written as follows:

$$x_{id}(t+1) = x_{id}(t) + v_{id}(t+1), \quad 1 \leqslant i \leqslant N; 1 \leqslant d \leqslant D. \tag{8}$$

$P_i = (p_{i1}, p_{i2}, \ldots, p_{iD})$ corresponds to the optimal position of the ith particle where it passes in the history and the best position $P_g = (P_{g_1}, P_{g_2}, \ldots, P_{g_D})$ of the gth particle is the best among all P_i $(i = 1, \ldots, N)$, c_1 and c_2 are positive constant numbers which can be called accelerating factors. $\mathrm{rand}()$ can be a random number among zero and one. u is an inertia weight factor. The bigger u fits the wider exploration among the solution space, and the smaller one fits exploitation in a smaller scope. The values of the position should be in a certain boundary $[-X_{\max d}, X_{\max d}]$ and the values of the velocity should be in a certain boundary $[-V_{\max d}, V_{\max d}]$. During the procedure of iteration, the values of position and velocity should be set to the boundary value if they are out of boundary. The initial population can be randomly produced and we can find the best position of the population during the process of iteration.

According to the basic principles listed above, the first task is how to represent the possible solution of a certain problem by the PSO algorithm. With the PSO algorithm, each particle represents possible phases of missing data close to the rigid bodies. First, after removing rotating parts, we need to consider how to express the missing STFT samples. As in [13], assuming the discrete FT (DFT) of the selected window is $w(k)$, e.g., hanning window, all the STFT samples corresponding to the frequency $k = k_r$ of the rigid bodies are equal to $w(0)$. Therefore, we can replace them with the median of the remaining STFT values. As we know, the missing STFT values have the form of $x_d(m) = w(d)\mathrm{e}^{\mathrm{j}2\pi md/M}$, for $k = d + k_r$, where $d \neq 0$. Their phases are different, but they have the same absolute value $W(d)$. For each frequency, after replacing the removed STFT values as the median of the rest STFT values close to k_r, we can choose their phases randomly from the set $[0, 2\pi)$.

For reconstructing the rigid bodies' FT, the rigid bodies' non-zero STFT values should be estimated for each time instant. It is known that, for each time instant, the selected window's FT can express the rigid body parts' STFT. The width of the hanning window has M_w points, centered at k_r. As we know, only three non-zero values exist in the DFT of the hanning window, but we need to make the used window zero-padded to meet M points. Thus, we should add non-zero STFT values to get the same frequency grid. We can calculate the number of additional non-zero values as follows:

$$|d| \leqslant 1 + 2(M/M_w - 1). \tag{9}$$

The initial non-zero value exists in each side of k_r, due to zero-padding, $M/M_w - 1$ non-zero values are between the initial value and zero, also between the initial value and non-zero value at $k = k_r$. In the reconstructed FT, we can determine the rigid body's position $k = k_r$ as the position of the maximum. Therefore, we can easily know the lost STFT values' amount and positions. If we remove 40% of STFT samples, each particle's length would be

$$L_p = 2[1 + 2(M/M_w - 1)]M_P \tag{10}$$

where $M_P = 50\%M$.

The second task is how to create the initial particle. This paper randomly chooses values of phases from $[0, 2\pi)$. The set of $[0, 2\pi)$ represents possible solutions.

The third task is to search the proper fitness function for all particles. The selection of the fitness function depends on the problem to be solved. In the context of our application we would get $S_{w1}(k) = \sum_{m=0}^{M-1} \mathrm{STFT}(m, k)$ after summing all the STFT values. It is the FT of the raw signal used window $w_1(i)$ which is a rectangular one in Sec-

tion 2. At the position k_r, there is just one non-zero value in the DFT result of the rigid bodies by using a rectangular window. Therefore, for evaluating the fitness of one particle, we can summing all the STFT values to reconstruct the FT, and the energy can be calculated as follows:

$$E = \sum_{\substack{|d|\leqslant 1+2(M/M_w-1)\\ d\neq 0}} |S_{w1}(k_r+d)|^2. \tag{11}$$

Equation (11) meets the conditions that k ranges from $k_r - d$ to $k_r \pm d$, $d \neq 0$, and $d \leqslant 1 + 2(M/M_w - 1)$ [22]. To obtain the estimate value of the missing values, we set them as the median of the rest STFT values. As we know, a peak at k_r with the zero values around means closer to the best solution for reconstructing FT of the rigid bodies. Therefore, the particle which owns the lower energy (11) has the higher fitness.

In this way, we have the fitness function. Then, some parameters should be set. Accelerating factors c_1, c_2 are both 2 and the velocity boundary is $[-2, 2]$. From the discussion above, the position boundary is $[0, 2\pi)$. In this paper, we adopt the linearly decreasing weight strategy to determine the value of inertia weight factor u, the form is shown as follows:

$$u(g) = (u_{\text{ini}} - u_{\text{end}})(G_k - g)/G_k + u_{\text{end}}. \tag{12}$$

In (12), G_k is the largest generation amount, g is the current generation amount, u_{ini} and u_{end} are always selected as 0.9 and 0.4.

The proposed procedure for reconstructing the missing STFT values of the rigid bodies is shown below, and Fig. 1 shows the flowchart of the PSO algorithm.

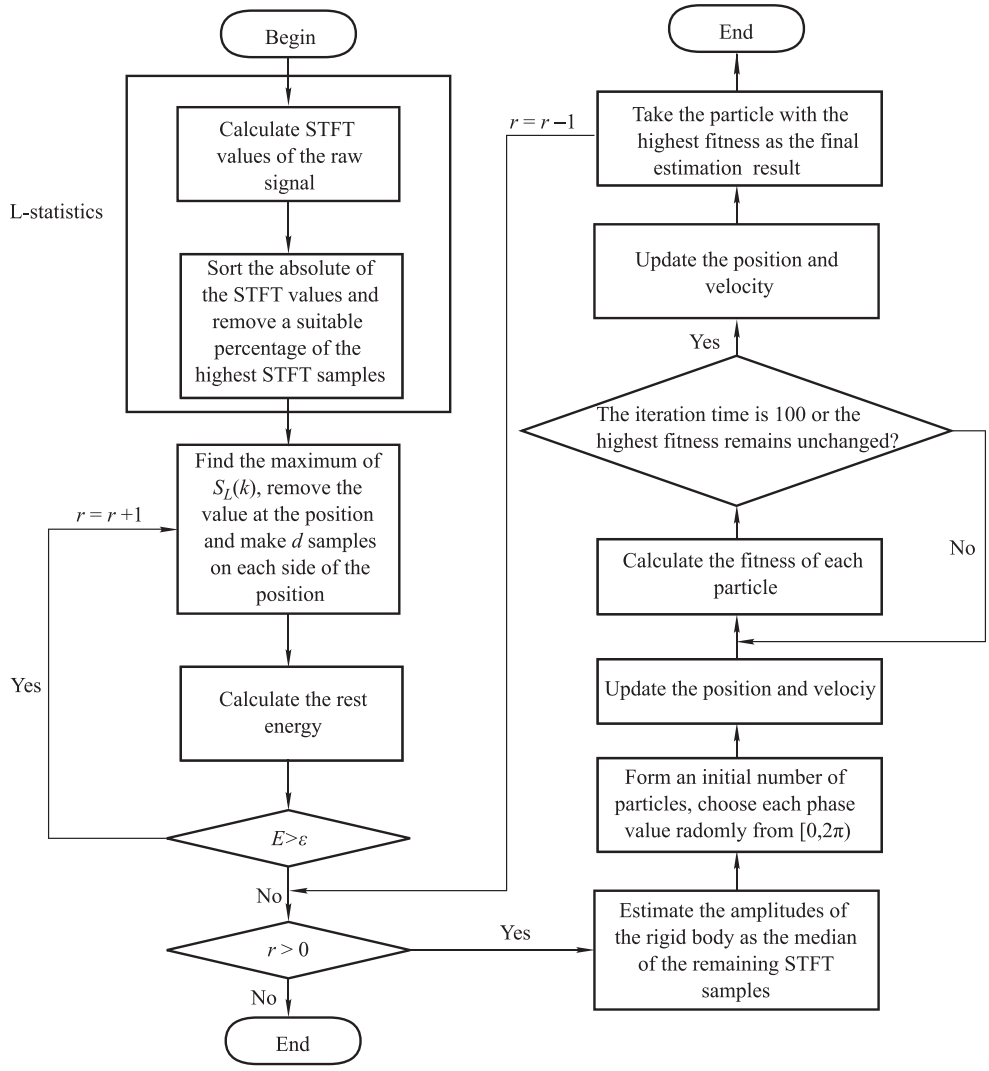

Fig. 1 Flowchart of PSO algorithm

Step 1 Calculate STFT values of the raw signal as (2). Then, the raw signal is converted from the time domain to the TF domain after STFT.

Step 2 Sort the absolute values of STFT and remove a suitable percentage (50% here) of the highest STFT samples based on STFT and L-statistics in each frequency bin.

Step 3 Sum the rest STFT values and get the reconstructed FT $S_L(k)$ as (6). Here, we set a threshold ε as 5% of the signal's energy with m-D removed and calculate the length of rigid body reflectors as in (9). The initial rigid body reflectors number r is set as 1. Find and record the maximum of $S_L(k)$ which corresponds to the rigid body reflector's position. Then, remove the value at the position and make d samples on each side of the position above.

Step 4 Compute the rest energy, if the energy value is higher than the threshold ε, let $r = r+1$, than go to Step 2. If not, go to Step 5.

Step 5 If $r > 0$, the missing values are estimated as the rest values' median along time dimension. On each side of the rigid body point, assuming there are no zero values at d frequencies, we can form an initial number of particles (100 particles) to be the generation, where each particle's position represents the phase of the non-zero missing rigid body values. Each phase value can be chosen randomly from the set $[0, 2\pi)$. If $r \leqslant 0$, go to the end.

Step 6 Update the position and velocity as in (7) and (8).

Step 7 Calculate each particle's fitness as (11).

Step 8 For iteration time of 100 or until the highest fitness remains unchanged, select the best particle according to the fitness function. Otherwise, go to Step 6.

Step 9 To get the final estimation result of the missing rigid body's phases, we choose the particle with the highest fitness from the last generation, here the missing rigid body values are non-zero. Finally, we sum all the recovered samples along the time dimension to get the FT of reconstructed rigid body samples and take it as the final estimation of S_{w1}. Let $r = r - 1$ and go to Step 5.

3.2 Computational complexity analysis of method based on PSO and GA

In [13], the method based on STFT and L-statistics was proved easier to apply than other methods, but the phenomenon of the rigid body loss can affect the imaging results. Reference [14] and this paper propose the GA and PSO for rigid body reconstruction, respectively. The computational complexity analysis of the GA and PSO are given here.

As hot multi-dimensional optimization algorithms are based on the biological evolution, GA and PSO are both stochastic processes, the calculation complexity cannot be given precisely. Generally, if the GA algorithm determines the population size and the PSO algorithm determines the particle swarm size, the number of fitness function calculations is the product of the population size and the number of generations. Although the number of generations cannot be determined precisely, the worst case can be determined. Suppose the number of generations is 100, the number of initialized individuals is 100, the number of fitness function calculations are both 100×100 for the GA and PSO. Then, the calculation complexity analysis is given for each generation. For the PSO, each individual size has 11 520 phase values. Each individual should update its speed and position, including five times of multiplication operations and five times of addition operations. After updating, the fitness function can be directly calculated. For the GA, the phase has to be encoded by three bits of the binary code to get the individual, which is $11\ 520 \times 3 = 34\ 560$. In the selection process of the GA, 20 individuals are selected to participate in the competition each time, new individuals are obtained after 19 comparisons, so there are 1 900 comparisons. In the process of crossover, 70% of the data are crossed and each bit of the two individuals is randomly assigned to the new children. Each assignment is equivalent to two binary additions. In the process of mutation, there is a 25% probability of one digit mutation per 50 digits, which means that the average number of binary additions performed is 17 280. Finally, before calculating the fitness function, the individual obtained needs to be decoded in binary and decoded into the decimal floating point number to calculate the energy.

In conclusion, due to more individual values, crossover and mutation of the GA, the calculation complexity is much higher than that of the PSO. Therefore, the proposed algorithm is better at computational complexity than the GA.

4. Simulations results

This section will show many simulations to verify the effectiveness of the PSO algorithm. We consider three types of simulation experiments, including signal simulations, ISAR imaging simulation and measured data test. To compare the results and the calculation amount of the GA and PSO, we set the same algorithm end condition on the same computer with an i7 processor. When the generation number reaches 100 or the highest fitness remains unchanged for consecutive five generations, the algorithm stops for both GA and PSO.

4.1 Signal simulations

The signal simulations include four examples, and all the examples are modeled as (1).

Example 1 In the first example, we consider the signal simulation of only one stationary and one rotating reflector, the discrete form of the signal can be written as follows:

$$s(m) = \mathrm{e}^{\mathrm{j}\cdot 0.5\pi m} + 20\mathrm{e}^{\mathrm{j}\cdot 80\cos(2\pi m/256)}. \tag{13}$$

The raw signal's STFT result is presented in Fig. 2(a), and the window is the hanning window, with $M_w = M/8$. We can see clearly that the frequency of the rigid bodies is constant, and partially covered by the m-D effects produced by rotating parts, which changes in a wide range of frequencies in the TF domain. Fig. 2(e) shows the FT result of the raw signal. We cannot distinguish the rigid body and rotating parts due to the m-D effects, thus we have to remove the m-D parts. Set removal percentage as 50% for each frequency, then remove the percentage above of the highest samples, the STFT result is obtained in Fig. 2(b). Although the m-D parts are cleared, quite a bit of rigid body samples are also missing. The rigid body reconstruction result by the GA is shown in Fig. 2(c). After using the proposed algorithm in this paper, the STFT values are reconstructed in Fig. 2(d). The FT result after L-statistics is presented in Fig. 2(f). We can see that a highly concentrated component exists with many low-concentrated values around, where the high concentrated component and low-concentrated values correspond to the rigid bodies and missing values of the rigid bodies. Summing the recovered STFT after GA and PSO, the FT is shown in Fig. 2(g) and Fig. 2(h), respectively. We can see that the residual spreading around the highly concentrated component is avoided effectively. Table 1 shows the operation time comparison of the GA and PSO. It can be clearly seen that the reconstruction effect of the rigid body is almost the same, but the operation time is much shorter.

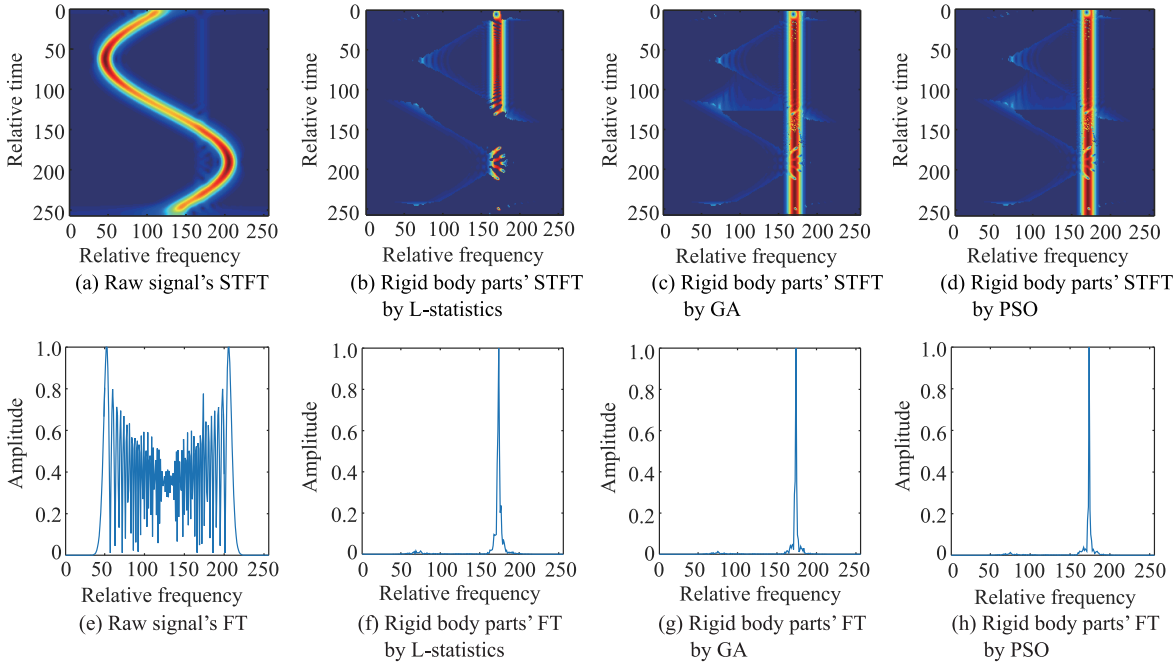

Fig. 2 Signal simulation of one stationary and one rotating reflector

Table 1 Operation time comparison result of Example 1

Item	Method	
	GA	PSO
Operation time/s	49.38	7.48

Example 2 For testing the performance of the proposed method to the noise environment, we use the same raw signal form of Example 1. For considering the noise influence, in the raw signal, we introduce white Gaussian noise, and the signal noise ratio (SNR) is set to –7.5 dB. Then, the STFT result and the FT result of the raw signal are presented in Fig. 3(a) and Fig. 3(e), respectively. In the figures, it can be seen that the energy of the rigid body is too weak to find. For each frequency, the percentage threshold is also 50%. The rigid body parts' STFT results by L-statistics, GA and PSO are obtained in Fig. 3(b), Fig. 3(c), Fig. 3(d), respectively. After the GA and PSO, the missing STFT values are recovered. As in Fig. 3(g) and Fig. 3(h), the rigid body parts' FT after the GA and PSO improves the concentration of the recovered FT compared to the FT result after m-D removal in Fig. 3(f). Table 2 shows the operation time comparison of the GA and PSO. The operation time of the PSO is shorter than that of the GA obviously.

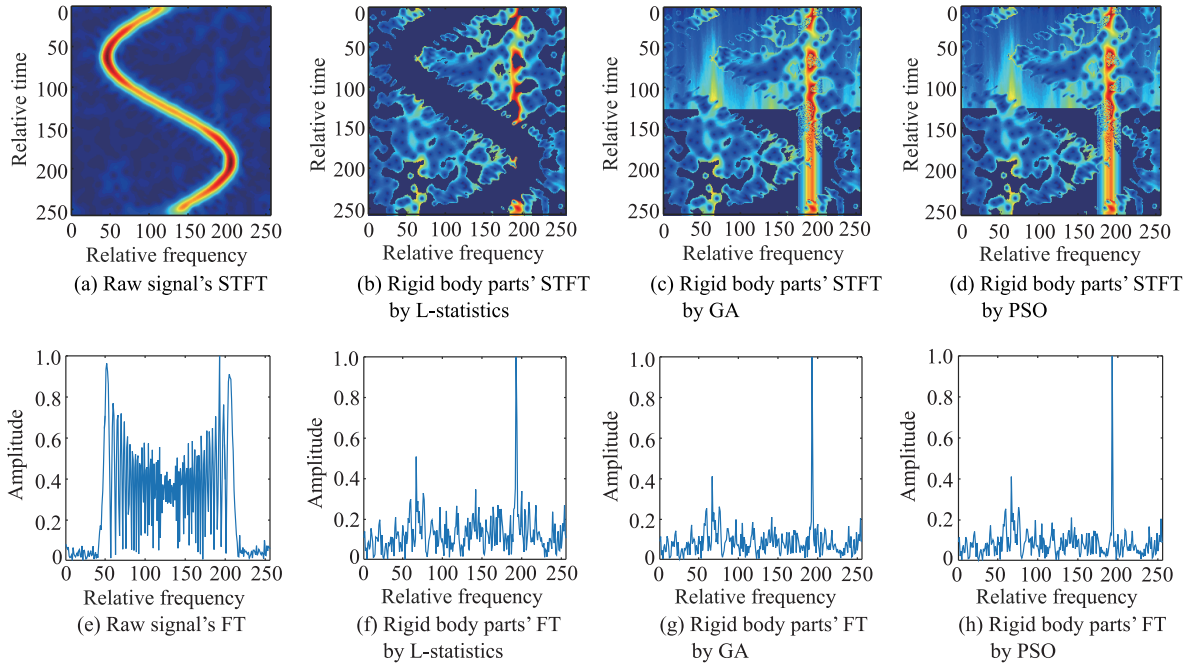

Fig. 3 Signal simulation of one stationary and one rotating reflector with noise

Table 2 Operation time comparison result of Example 2

Item	Method	
	GA	PSO
Operation time/s	112.94	9.08

Example 3 In this example, we consider the signal simulation of multiple stationary and multiple rotating reflectors. We assume the signal consists of six components in this example to test the performance of multiple signals. As in (1), set $K = 3$ and $Q = 3$, corresponding to three rigid body points and three rotating points. Equation (1) with $\sigma_{Bi} = 5$, $\sigma_{Ri} = 15$, $y_{Bi} = [1.5\pi, 2\pi, 2.5\pi]$, $y_{R0i} = 0$, and $A_{Ri} = [72, 84, 96]$, $\varphi_i = [-\pi/3, 0, \pi/3]$, $\omega_{Ri} = \pi/128$, for $i = 1, 2, 3$, $M = 256$, and $M_w = M/8 = 32$. In Fig. 4(a), the raw signal's STFT is shown, it can be seen that the rigid body parts have a constant frequency in the TF domain, but they are contaminated by the multiple patterns in sine form which is produced by the rotating reflectors.

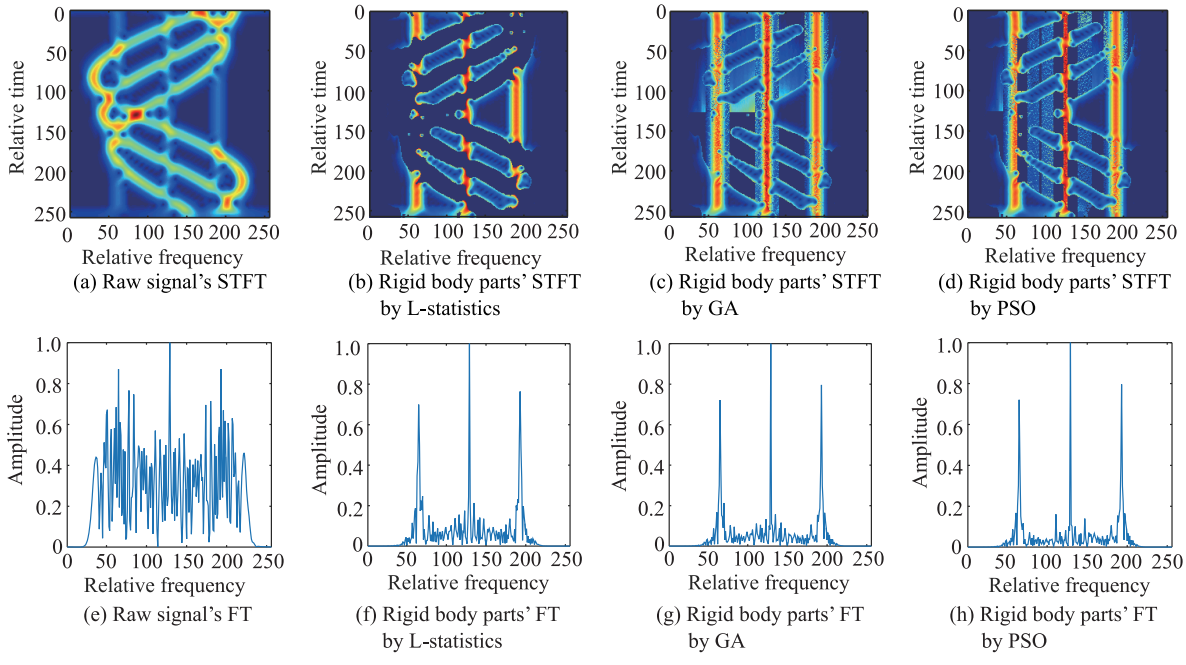

Fig. 4 Signal simulation of multiple stationary and multiple rotating reflectors

We cannot separate the rigid body from the raw signal's FT result as in Fig. 4(e). In this example, the m-D parts are also eliminated (see Fig. 4(b)). The rigid body parts' reconstructed FT based on L-statistics is shown in Fig. 4(f). We successfully recover all three rigid body reflectors. However, the three rigid body reflectors do not have three sharp peaks. Due to the missing STFT samples, there is residual spread. After using the GA and PSO algorithms, the STFT values filled with the estimated values are presented in Fig. 4(c) and Fig. 4(d), it can be clearly seen that the missing samples of the rigid bodies are reconstructed successfully. For the multiple rigid body reflectors, the GA and PSO algorithms can produce highly concentrated FT, the reconstructed FT results are shown in Fig. 4(g) and Fig. 4(h). Table 3 gives the operation time comparison of the GA and PSO. As in Table 3, PSO has obvious advantages in operation time.

Table 3 Operation time comparison result of Example 3

Item	Method	
	GA	PSO
Operation time/s	223.80	25.65

Example 4 In this example, we consider two close rigid bodies and one rotating reflector to analyze the high resolution of the proposed method. The signal form is shown as follows:

$$s(m) = 2\mathrm{e}^{-\mathrm{j}\cdot 120\pi m/M} + 3\mathrm{e}^{-\mathrm{j}\cdot 125\pi m/M} + 10\mathrm{e}^{\mathrm{j}\cdot 30\cos(2\pi m/M)} \tag{14}$$

where $M = 256$, set the width of the window as $M_w = M/4$, which can ensure the higher resolution of close rigid bodies. Fig. 5(a) shows the STFT of the raw signal, while the raw signal's FT is shown in Fig. 5(e). In Fig. 5(e), we cannot clearly distinguish the two close rigid bodies. After removing 50% of the highest STFT values, the result is obtained in Fig. 5(b), then we can get the FT of the rigid body parts in Fig. 5(f) by summing the rest STFT values. We can see that the two rigid bodies are still difficult to be distinguished. Using the GA and the proposed method, the results are presented in Fig. 5(c), Fig. 5(d), Fig. 5(g) and Fig. 5(h). From the figures, it is easy to distinguish the two close rigid bodies and verify the high resolution performance of the proposed method. The operation time comparison of the GA and PSO is given in Table 4. Similarly, the PSO has shorter operation time.

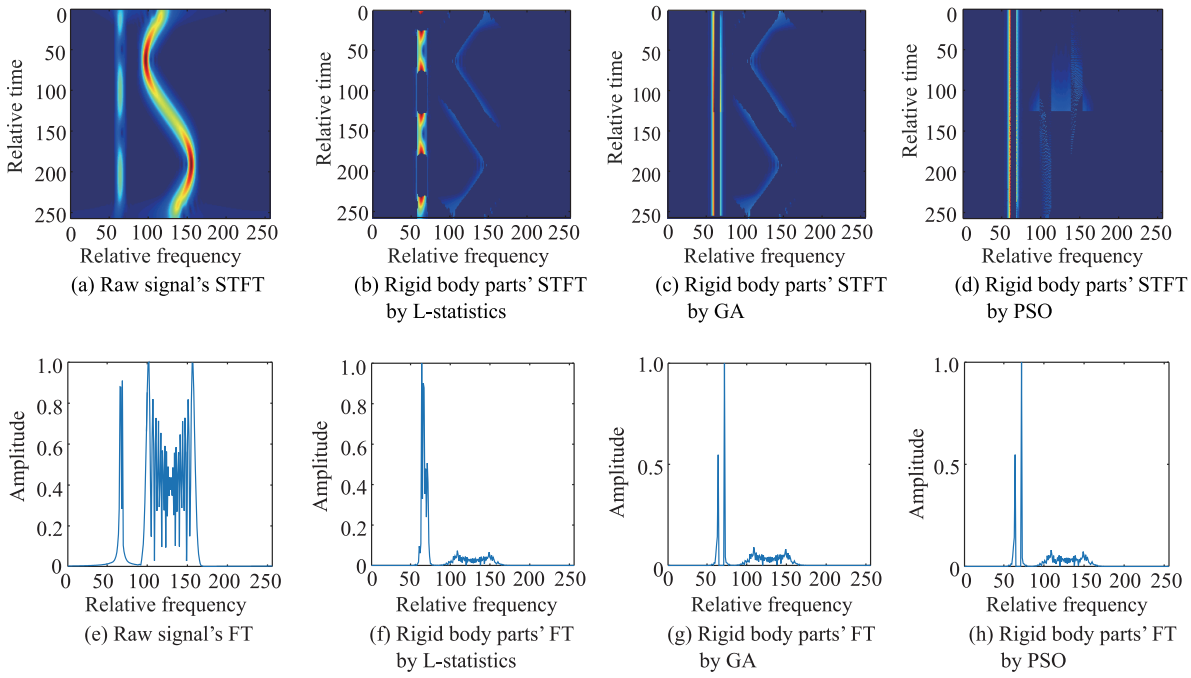

Fig. 5 Signal simulation of two close rigid bodies and one rotating reflector

Table 4 Operation time comparison result of Example 4

Item	Method	
	GA	PSO
Operation time/s	42.65	9.94

4.2 ISAR imaging simulations

Example 5 In this example, to show the influence of m-D effect, we simulate ISAR imaging by the point-scatterer model. The target's point-scatterer model is pre-

sented in Fig. 6. The rigid body scatterers 1 – 8 rotate around the center (0, 0) with the angular speed of 0.2 rad/s. Scatterer 9 corresponding to rotating parts locates in (0, 0), and rotates around the center with the rotational of 6.67 Hz. The radar frequency is 10 GHz, and the bandwidth is 300 MHz, the observation distance is 1 000 m, the time width is 25.6 μs, and the pulse repetition frequency (PRF) is 2 000 Hz. In this example, 512 echoes and 128 range samples are chosen as the original signal during the target imaging time.

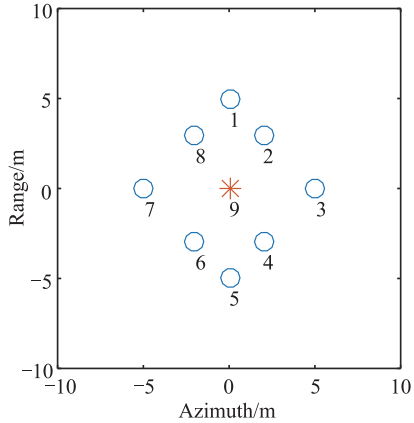

Fig. 6 Target's point-scatterer model

After using the traditional range-Doppler (RD) algorithm, the ISAR image is presented in Fig. 7(a). We can see that the images of the rigid body scatterer 1 and scatterer 5 are shadowed by the m-D effect of scatterer 9 near the range cell of 65. Thus, we take the range cell of 65 as an example. Fig. 7(b) presents the normalized autocorrelation coefficient of the original data. We can see that the interval of peak is about 0.15 s, which corresponds to the rotation frequency of 6.67 Hz. The STFT results at the range cell of 65 with hanning window are shown in Fig. 7(c). We can see that rigid body scatterers 1 and 5 have the form of the horizontal lines in the TF domain and the rotating scatterer 9 appears as sinusoidal curve in the TF domain, thus they are easily identified. After the GA and PSO algorithms for all the range cells, the reconstructed ISAR image results are presented in Fig. 7(e) and Fig. 7(f). We can see that the m-D effect is removed correctly and the image is well-focus. The reconstructed ISAR image by m-D removal based on L-statistics is shown in Fig. 7(b). All the rigid body parts are recovered, but there are still some rotating scatterer remaining samples and the rigid body reflectors are not well focused.

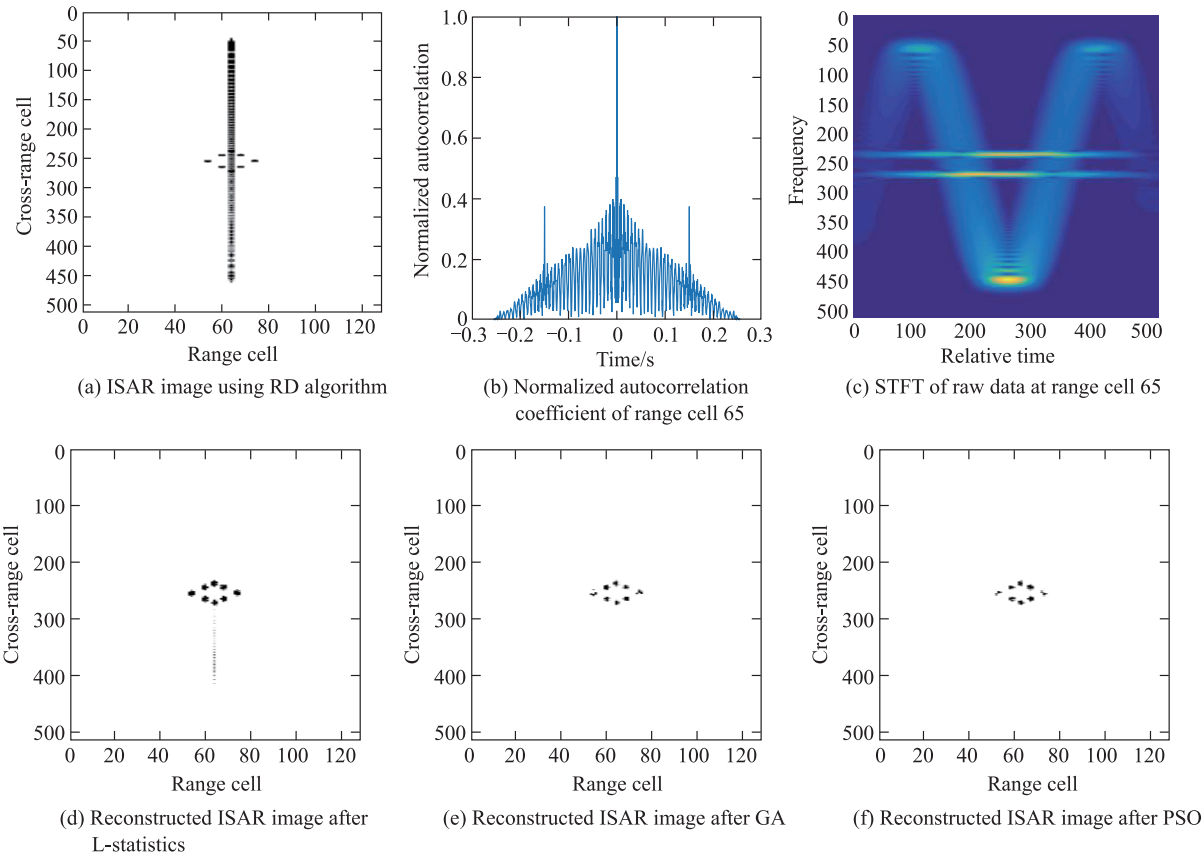

(a) ISAR image using RD algorithm

(b) Normalized autocorrelation coefficient of range cell 65

(c) STFT of raw data at range cell 65

(d) Reconstructed ISAR image after L-statistics

(e) Reconstructed ISAR image after GA

(f) Reconstructed ISAR image after PSO

Fig. 7 Simulation of point-scatterer model

We introduce the entropy of the image to measure the imaging quality. We can know that a better focused imaging has a smaller entropy [23]. Then, we can compute the entropies of the images in Fig. 7(e) and Fig. 7(f). The entropy for an image $p(m,n)$ is defined as follows:

$$E=\sum_{m=0}^{M-1}\sum_{n=0}^{N-1}\frac{|p(m,n)|^2}{Q}\ln\frac{Q}{|p(m,n)|^2} \tag{15}$$

where $Q=\sum\limits_{m=0}^{M-1}\sum\limits_{n=0}^{N-1}|p(m,n)|^2$, $0\leqslant m\leqslant M-1$, and $0\leqslant n\leqslant N-1$.

The comparison results between the L-statistics, GA and PSO in different signal-noise ratios (SNR) are shown in Table 5, the operation time of the GA and PSO is also compared. From the comparison results, it can be seen that the entropies of ISAR images using the GA and PSO algorithms are less than those using L-statistics.

It proves that the quality of the image using the rigid body reconstruction algorithm is better than L-statistics without rigid body parts reconstructing. At the same time, it can be seen that the imaging entropy values of the GA and PSO are almost the same, but the operation time of the PSO is much shorter than that of the GA.

Table 5 Entropy of image and operation time comparison results

SNR	Image entropy			Operation time/s	
	L-statistics	GA	PSO	GA	PSO
−10	5.061 9	4.012 3	3.983 8	2 120.52	150.32
−5	4.680 2	3.721 9	3.741 9	1 850.24	135.23
0	4.501 6	3.382 2	3.371 7	1 324.60	120.65
5	4.426 4	3.225 0	3.236 6	1 250.54	115.84
10	4.402 0	3.145 2	3.083 7	1 098.42	102.41

4.3 AN-26 measured data test

Example 6 This example is to verify the effect of the PSO algorithm with measured data of a short range conveyer AN-26. The fuselage of AN-26 plane is 23.8 m with two turbos on each side of the airframe. Fig. 8 shows the framework of the AN-26 plane [24]. In the measured data, the bandwidth of the radar is 400 MHz, and the PRF is 400 Hz. The ISAR image using the RD algorithm is shown in Fig. 9(a). We can see that the image of the rigid bodies is clearly contaminated by m-D interference produced by the two propellers over the whole spectrum. The STFT results of the echo in range cell 150 are presented in Fig. 9(b).

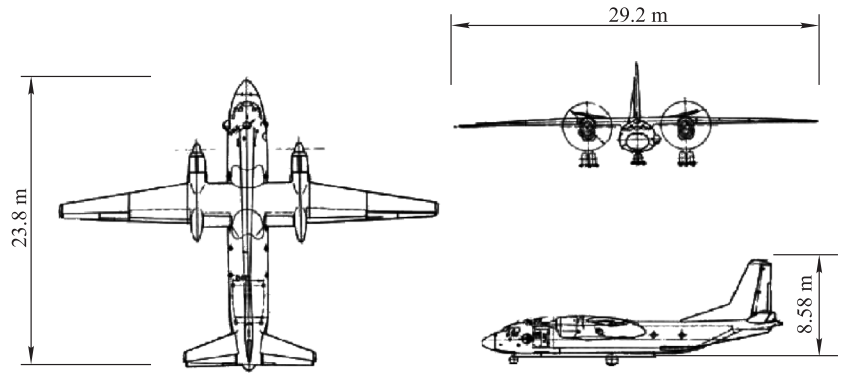

Fig. 8 Framework of the AN-26 plane

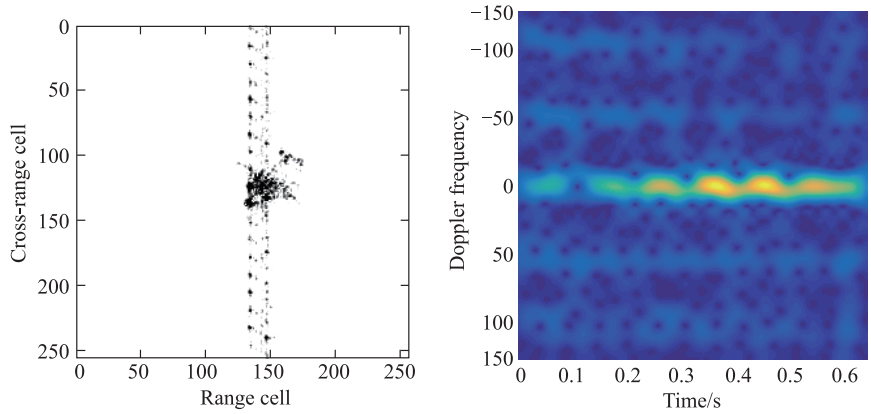

(a) ISAR image by RD algorithm (b) STFT in range cell 150

Fig. 9 Results of the AN-26 plane measured data

It can be observed that the Doppler of the rigid body parts is approximately constant, which exists around zero frequency. However, the m-D effect of the two propellers occupies the whole spectrum whose characteristic is difficult to identify. Fig. 10(a) shows the reconstructed ISAR image based on L-statistics. We can see that the effect of m-D is weakened, but it is still serious. After using the method based on the PSO algorithm, the target image is reconstructed in Fig. 10(c). It is clear that the effect of m-D is greatly diminished and the wings of the AN-26 plane is well-focused.

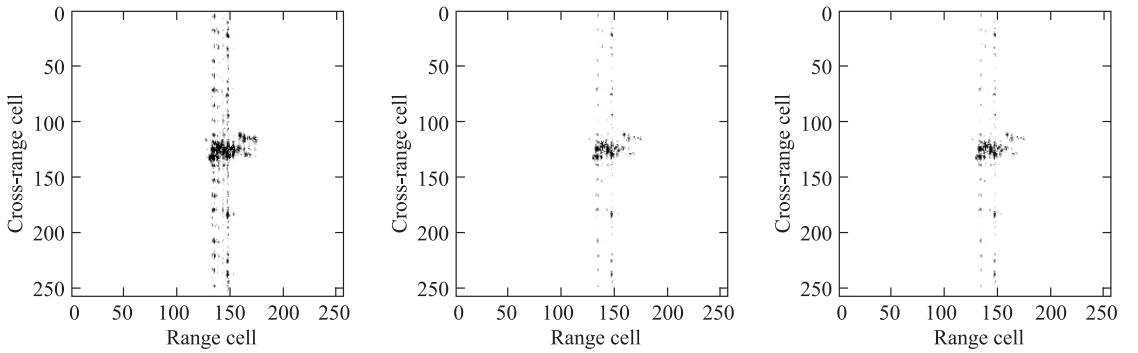

(a) Reconstructed ISAR image by L-statistics (b) Reconstructed ISAR image by GA (c) Reconstructed ISAR image by PSO

Fig. 10 ISAR image of AN-26 plane after m-D separation

We also compute the entropies of the ISAR images of Fig. 10 and Fig. 10(c) to compare their image quality, and record the operation time for each algorithm. In Table 6, the comparison result is presented. It is clear that the entropies of the AN-26 ISAR images using the GA and PSO algorithms are less than those using L-statistics. Compare the GA and the PSO, the entropy values of the AN-26 ISAR image are very close, but the PSO algorithm has obvious advantages in the operation time. This result also verifies the excellent image quality and low computational cost of the PSO algorithm.

Table 6 Entropy of AN-26 ISAR image and operation time comparison results

Image entropy			Operation time/s	
L-statistics	GA	PSO	GA	PSO
5.346 7	4.537 0	4.548 4	1 739.48	167.56

5. Conclusions

The m-D effect appears when a target has rotating parts in ISAR imaging. This phenomenon can severely decrease the quality and readability of the obtained ISAR image, and make the rigid body parts difficult to detect. This paper proposes the PSO algorithm with the low computational cost to recover the missing data close to rigid body parts for removing the m-D effects better. The results of the signal simulations, ISAR image simulation and AN-26 plane measured data verify the validity and accuracy of the proposed method.

References

[1] CHEN V C, LI F, HO S S, et al. Analysis of micro-Doppler signatures. IEE Proceedings Radar, Sonar and Navigation, 2003, 150(4): 271 – 276.

[2] CHEN V C. Micro-Doppler effect in radar: Part I: phenomenon, physics, mathematics, and simulation study. IEEE Trans. on Aerospace and Electronic Systems, 2006, 42(1): 2 – 21.

[3] BAI X, ZHOU F, XING M, et al. High resolution ISAR imaging of targets with rotating parts. IEEE Trans. on Aerospace and Electronic Systems, 2011, 47(4): 2530 – 2543.

[4] TOTIR F, RADOI E. Superresolution algorithms for spatial extended scattering centers. Digital Signal Processing, 2009, 19(5): 780 – 792.

[5] MARTORELLA M. Novel approach for ISAR image cross-range scaling. IEEE Trans. on Aerospace and Electronic Systems, 2008, 44 (1): 281 – 294.

[6] MARTORELLA M, BERIZZI F. Time windowing for highly focused ISAR image reconstruction, IEEE Trans. on Aerospace and Electronic Systems, 2005, 41(3): 992 – 1007.

[7] WANG Y, JIANG Y C. ISAR imaging of ship target with complex motion based on new approach of parameters estimation for polynomial phase signal. EURASIP Journal on Advances in Signal Processing, 2011, 2011: 1 – 9.

[8] THAYAPARAN T, ABROL S, RISEBOROUGH E, et al. Analysis of radar micro-Doppler signatures from experimental helicopter and human data. IET Radar, Sonar and Navigation, 2007, 1(4): 288 – 299.

[9] LI J, LING H. Application of adaptive chirplet representation for ISAR feature extraction from targets with rotating parts. IEE Proceedings Radar, Sonar and Navigation, 2003, 150(4): 284 – 291.

[10] THAYAPARAN T, SURESH P, QIAN S. Micro-Doppler analysis of rotating target in SAR. IET Signal Processing, 2010, 4(3): 245 – 255.

[11] STANKOVIC L, THAYAPARAN T, DJUROVIC I. Separation

of target rigid body and micro-Doppler effects in ISAR imaging. IEEE Trans. on Aerospace and Electronic Systems, 2006, 42(4): 1496 – 1506.
[12] THAYAPARAN T, STANKOVIC L, DJUROVIC I. Micro-Doppler based target detection and feature extraction in indoor and outdoor environments. Journal of the Franklin Institute, 2008, 345(6): 700 – 722.
[13] STANKOVIC L, THAYAPARAN T, DAKOVIC M, et al. Micro Doppler removal in the radar imaging analysis. IEEE Trans. on Aerospace and Electronic Systems, 2013, 49(2): 1234 – 1250.
[14] STANKOVIC L, BUGARIN V P, RADENOVIC F. Genetic algorithm for rigid body reconstruction after micro-Doppler removal in the radar imaging analysis. Signal Processing, 2013, 93(7): 1921 – 1932.
[15] KENNEDY J, EBERHART R. Particle swarm optimization, neural networks. Proc. of the International Conference on Neural Networks, 1995: 1942 – 1948.
[16] BRINKMAN W, THAYAPARAN T. Focusing ISAR images using the AJTF optimized with the GA and the PSO algorithm. Proc. of the IEEE Conference on Comparison and Results, Radar, 2006: 510 – 517.
[17] SHI Y H, EBERHART R. A modified particle swarm optimizer, evolutionary computation. Proc. of the IEEE World Congress on Computational Intelligence, 1998: 69 – 73.
[18] DJUROVIC I, STANKOVIC L, BOHME J F. Robust L-estimation based forms of signal transforms and time-frequency representations. IEEE Trans. on Signal Processing, 2003, 51(7): 1753 – 1761.
[19] WANG Y, KANG J. Parameter estimation for rigid body after micro-Doppler removal based on L-statistics in the radar analysis. Journal of Systems Engineering and Electronics, 2015, 26(3): 457 – 467.
[20] LIU L, QI M S, ZHOU F. A novel non-uniform rotational motion estimation and compensation method for maneuvering targets ISAR imaging utilizing particle swarm optimization. IEEE Sensors Journal, 2018, 18(1): 299 – 309.
[21] LIU L, ZHOU F, TAO M L, et al. Adaptive translational motion compensation method for ISAR imaging under low SNR based on particle swarm optimization. IEEE Journal of Selected Topics in Applied Earth Observations and Remote Sensing, 2015, 11(8): 5146 – 5157.
[22] STANKOVIC L. A measure of some time – frequency distributions concentration. Signal Processing, 2001, 81(3): 621 – 631.
[23] WANG Y, KANG J, JIANG Y C. ISAR imaging of maneuvering target based on the local polynomial wigner distribution and integrated high-order ambiguity function for cubic phase signal model. IEEE Journal of Selected Topics in Applied Earth Observations and Remote Sensing, 2014, 7(7): 2971 – 2991.
[24] YUAN B, CHEN Z P, XU S Y. Micro-Doppler analysis and separation based on complex local mean decomposition for aircraft with fast-rotating parts in ISAR imaging. IEEE Trans. on Geoscience and Remote Sensing, 2014, 52(2): 1285 – 1298.

Biographies

LI Hongzhi was born in 1987. He received his B.S. degree and M.S. degree in electronic information engineering and underwater acoustic engineering from Harbin Engineering University in 2010 and 2013, respectively. He is currently an engineer of School of Electronics and Information Engineering and an on-the-job doctoral candidate at Harbin Institute of Technology (HIT). His main research interests include radar imaging technology, high frequency radar frequency selecting and frequency monitoring system anti-interference, and inverse synthetic aperture radar imaging.
E-mail: lihongzhi2014@hit.edu.cn

WANG Yong was born in 1979. He received his B.S. and M.S. degrees in electronic engineering from Harbin Institute of Technology (HIT), Harbin, China, in 2002 and 2004, respectively. He received his Ph.D. degree in information and communication engineering from HIT in 2008. He is currently a professor with the Institute of Electronic Engineering Technology in HIT. His research interests include time frequency analysis of nonstationary signal, radar signal processing, and their application in synthetic aperture radar (SAR) imaging.
E-mail: wangyong6012@hit.edu.cn